EFFECTS OF THE SiO$_2$-B$_2$O$_3$ RATIO ON THE STRUCTURE AND PROPERTIES OF B$_2$O$_3$-ZnO-SiO$_2$-BaO-LiO$_2$-Al$_2$O$_3$-Na$_2$O-CaO PARENT GLASS AND GLASS-CERAMICS

ZIJIE LI*, FENG HE*,#, CONGCONG ZHENG*, DONGYANG YAN*, BING ZHANG*,
XIUHUA CAO**, HAIDONG REN**, JUNLIN XIE*

*State Key Laboratory of Silicate Materials for Architectures, Wuhan University of Technology, Wuhan 430070, China
**State Key Laboratory of Advanced Materials and Electronic Components, LTD of Guang Dong Feng Hua, Guangdong,
Zhaoqing 526000, China

#E-mail: he-feng2002@163.com

The experimental results show that a decrease in the SiO$_2$/B$_2$O$_3$ ration reduced the glass transition temperature, but had little effect on the crystallisation temperature. The basic glass powder pressed into strip samples were sintered at a temperature of 630 to 690 °C. With a decrease in the SiO$_2$/B$_2$O$_3$ ratio, the structure of glass and glass-ceramics changed, and the same change also occurred in the crystal phase in the glass-ceramics. When the SiO$_2$/B$_2$O$_3$ ratio was 0.29, the glass-ceramics sintered at 670 °C reached the best properties, including the bending strength, density, and acid resistance. When the SiO$_2$/B$_2$O$_3$ ratio was 0.29, the coefficient of thermal expansion of the glass-ceramics sintered at different temperatures were maintained in the range of 6.3 – 7.2 × 10^{-6} K^{-1}.

INTRODUCTION

Electronic devices have become the core equipment for many scientific and technological apparatus in today's high-tech era due to their quality which directly affects the overall performance of the electronic equipment [1]. Electronic pastes are indispensable in the process of making electronic devices. They are mainly used in the packaging, electrodes and interconnecting materials of electronic devices, and are one of the core materials in the preparation of electronic devices [2, 3]. An electronic paste can be used in the production of many important electronic devices, such as capacitors, integrated circuits, optoelectronic devices, potentiometers, and semiconductors [4]. The electronic paste is usually added by screen printing on the surface of the ceramic substrate, and after a high temperature treatment, the electronic paste will solidify on the substrate surface and form a thick film [5, 6]. A typical electronic paste contains a conductive metal powder, a binder, and an organic solvent [7]. Glass powders are usually used as a binder because of their low cost, strong bonding with ceramics and adjustable thermal expansion [1, 8, 9]. The main function of glass powders is to adhere the conductive metal powder and the substrate during

the sintering process, so the performance of the sintered glass powder directly affects the applicability of the electronic paste to electronic devices [10]. The electronic paste for the packaging of electronic devices made from different materials will be affected by the wettability and adhesion of the binder to the substrate. In addition, if the applicable sintering temperature of the glass powder is too high, the electronic devices will be damaged during the packaging process [11]. In this context, a glass with a low sintering temperature, good sintering compactness and good thermal expansion has been studied.

At present, the research on low-temperature sintering glass has been applied to the sealing of solid oxide fuel cells and the application of low temperature co-fired ceramics [12-14], but there is little research focused on electronic paste glass powders. Borate-based glass has strong chemical stability and has many applications in low temperature co-fired ceramics, and it can be easily combined with ceramic materials commonly used in electronic devices, such as alumina and barium titanate [13, 15, 16].

In this work, borate-based glass was selected to study the structure and properties of a low-temperature sintering glass. The parent glass was obtained by melting raw materials and naturally cooling glass blocks,

and the ball-milled glass powders were sintered at a specific temperature. We explored the effect of the SiO_2/B_2O_3 ratio on the structure of the parent glass and glass-ceramics, as well as the effect of the structure on the properties of the glass-ceramics.

EXPERIMENTAL

Sample preparation

The main raw materials in this experiment were chemically pure H_3BO_3, ZnO, SiO_2, $BaCO_3$, Li_2O, Al_2O_3, Na_2CO_3, and $CaCO_3$. The materials were weighed according to Table 1, and they were thoroughly mixed. They were melted in alumina crucibles at 1350 °C for 1 hour, in a high temperature furnace at a rate of 2 °C·min⁻¹. The glass blocks were obtained after the melts were rapidly flattened onto a pre-placed mould and naturally cooled to room temperature. After the glass blocks were crushed, zirconia grinding balls were added in a planetary mill at a ratio of 2 times the glass, and the glass was ground at a speed of 350 rpm for 16 hours. After passing through 500-mesh sieves, the glass powders with an appropriate amount of a 5 % Polyvinyl Alcohol (PVA) solution were pressed into the form of rectangular bars (40 mm × 6 mm × 6 mm) under 10 MPa of pressure. To prepare the sintered glass-ceramics, a high-temperature furnace was used to sinter the strip samples at 630 °C, 650 °C, 670 °C, and 690 °C at a heating rate of 10 °C·min⁻¹. The sintering atmosphere was air and the holding time was 10 minutes.

Testing and characterisation

The infrared spectra of the parent glass and the glass-ceramics were recorded with a Nicolet 6700 spectrometer at room temperature in a range of 400 – 1600 cm⁻¹. The crystalline phases of the glass-ceramics were determined by X-ray diffraction ((XRD), D8 Advance, Bruker AXS, Germany) with a Cu Kα radiation source. The samples were scanned over a 2θ range of 10 – 70 °. A differential scanning calorimeter ((DSC), STA449F3) was used to measure the characteristic temperatures of the glass from room temperature to 1000 °C in the air, at a heating rate of 10 °C·min⁻¹. The ²⁹Si MAS NMR spectroscopy used an AVANCE III solid magnetic resonance spectrometer produced

by Bruker, Germany. A DIL 402C dilatometer produced by Netzsch, Germany was used to measure the coefficient of thermal expansion (CTE) of the strip samples, where the heating rate was 10 °C·min⁻¹ and the atmosphere was air. The bending strength was tested using the three-point test method in a universal testing machine with instrument model KZY-300-1, and the final result was the average of five samples. The density was tested using the Archimedes drainage method, and the data were the average of six test results. A Zeiss Ultra Plus field emission scanning electron microscope manufactured by Zeiss, Germany, with an X-Max 50 X-ray energy spectrometer, was used to scan and analyse the samples before and after the acid resistance test. The acid resistance test used 10 wt. % hydrochloric acid (HCl) to soak the samples for half an hour, and the results were the average of three tests.
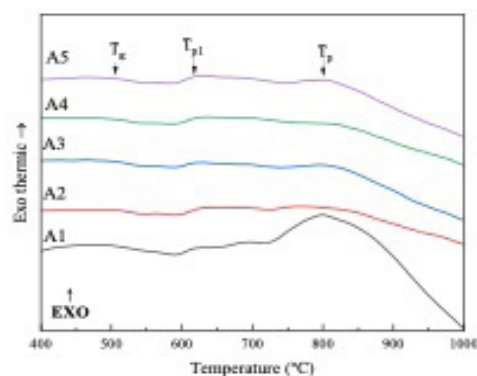

Figure 1. DSC of the parent glasses with different SiO_2/B_2O_3 ratios.

Table 1. The compositions of the parent glass (wt. %).

Sample	B_2O_3	ZnO	SiO_2	BaO	Li_2O	Al_2O_3	Na_2O	CaO	SiO_2/B_2O_3
A1	38.00	35.00	15.00	5.00	2.00	2.00	2.00	1.00	0.39
A2	39.00	35.00	14.00	5.00	2.00	2.00	2.00	1.00	0.36
A3	41.00	35.00	12.00	5.00	2.00	2.00	2.00	1.00	0.29
A4	42.00	35.00	11.00	5.00	2.00	2.00	2.00	1.00	0.26
A5	43.00	35.00	10.00	5.00	2.00	2.00	2.00	1.00	0.23

RESULTS AND DISCUSSIONS

DSC analysis

Figure 1 shows the DSC results of the A1 – A5 parent glasses. Table 2 shows the special temperature points of the A1 – A5 parent glasses. It can be seen from Figure 1 that the T_g (glass transition temperature) of the A series glass was in a range of 520 – 530 °C. The first crystallisation temperature (T_{p1}) was in a range of 617 – 627 °C, and the second crystallisation temperature (T_{p2}) was in a range of 788 – 800 °C. When the glass sample is heat-treated at the crystallisation temperature, crystals will form inside the glass and grow with an increase in the holding time or the sintering temperature.

The T_g was related to the complexity of the internal network of the glass. The decrease of the T_g in Table 2 means that the decrease in the relative SiO_2 content had

Table 2. DSC characteristic temperature points of the parent glasses with different SiO_2/B_2O_3 ratios.

Number	A1	A2	A3	A4	A5
T_g (°C)	528	525	523	523	522
T_{p1} (°C)	619	627	621	617	627
T_{p2} (°C)	800	788	806	800	799

changed the glass network structure. The crystallisation temperature of the samples fluctuated with the change in the composition content, and the range was small, which meant that the change in the SiO_2/B_2O_3 ratio had little effect on the crystallisation temperature of this series of glass. From the DSC analysis of the A1 – A5 parent glasses, it can be seen that the T_{p1} of those parent glasses was about 620 °C. In order to observe the transformation of the internal structure of the glass-ceramics, the glass powders were sintered at 630 °C, 650 °C, 670 °C, and 690 °C.
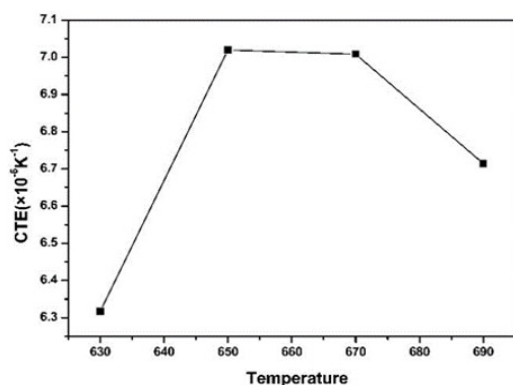
Figure 2. CTE of the A3 glass-ceramic sintered at different temperatures.

Thermal expansion analysis

It can be seen from Figure 2 that the thermal expansion of the A3 sintered glass at different temperatures first increases and then decreases. The thermal expansion changed very little when the sintering temperature was between 650 °C and 670 °C, but decreased when the sintering temperature was higher than 670 °C or below 650 °C. The change in the sintering temperature affected the generation of the liquid phase and the formation of the crystalline phase in the glass during sintering. As the sintering temperature increased, the glass powder softened, and the volume shrunk to produce the densification. When the sintering temperature was higher than the softening temperature, a liquid phase was generated in the glass, which increases the compactness of the sintered glass.

However, a higher sintering temperature leads to a larger liquid phase produced in the glass, which causes the strip sample to collapse and change the thermal expansion of the sintered glass.
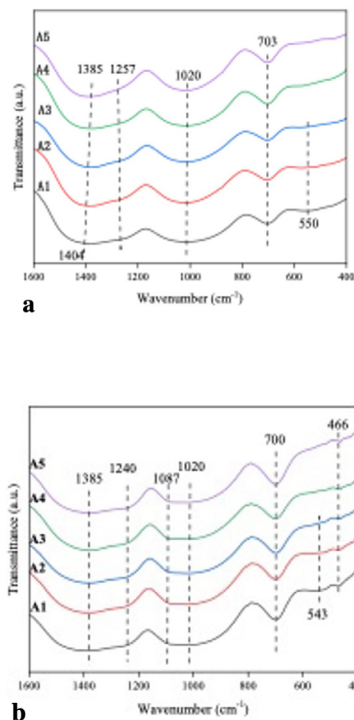
Figure 3. FTIR spectra of the parent glasses and glass-ceramics: a) FTIR spectra of the parent glasses, b) FTIR spectra of the glass-ceramics.

FTIR analysis

Figure 3a shows the infrared diffraction spectra of the parent glasses. It can be seen from Figure 3a that the absorption peak bands of the parent glasses can be divided into five bands, namely 550 cm^{-1}, 703 cm^{-1}, 1020 cm^{-1}, 1257 cm^{-1}, 1385 cm^{-1}. The absorption peak at 550 cm-1 was attributed to the vibration of $[AlO_6]$ [17]. The absorption peak at 703 cm^{-1} was attributed to the B-O-B bending vibration in $[BO_3]$ [18, 19]. The absorption peak at 1020 cm^{-1} was attributed to the asymmetric vibration of Si-O-Si in $[SiO_4]$ [17]. The absorption peak near 1257 cm^{-1} was attributed to the bending vibration of B-O in $[BO_3]$ [19]. The absorption peak at 1385 cm^{-1} was attributed to the vibration of B-O in $[BO_3]$ [20]. With a decrease in the SiO_2/B_2O_3 ratio, the infrared absorption peaks of the A1 to A5 parent glasses at 703 cm^{-1} – 1385 cm^{-1} did not change much. As the relative content of the SiO_2 decreased, the glass network became loose, and the absorption peak generated at 1385 cm^{-1} gradually shifted from a high band to a low band. The absorption peak at 550 cm^{-1} gradually disappeared as the relative content of the SiO_2 decreased. The decrease in the relative SiO_2 content changed

the degree of polymerisation of the anionic groups inside the glass, and the glass network structure also changed [21].

Figure 3b shows the infrared spectrum of the A1 to A5 glass-ceramics sintered at 670 °C. It can be seen from Figure 3b that the structure of the glass samples changed after sintering. The absorption peaks at 1020 cm⁻¹ and 1257 cm⁻¹ – 1385 cm⁻¹ were wider than those of the parent glasses. The absorption peak near 1257 cm⁻¹ deviated to 1240 cm⁻¹ [22], and became more obvious. The absorption peak at 550 cm⁻¹ deviated to around 543 cm⁻¹, the signal intensity was reduced, and the absorption peak of the A3 glass-ceramic disappeared. New absorption peaks were generated at 466 cm⁻¹ and 1087 cm⁻¹. The absorption peak generated at 466 cm⁻¹ was weak, and the signal source was attributed to the bending vibration of O-Si-O in [SiO₄] [17]. The absorption peak at 1087 cm⁻¹ was split from the absorption peak at 1020 cm⁻¹, and this signal corresponded to the Si-O-Si asymmetric stretching vibration in [SiO₄] [23]. The absorption peak at 1385 cm⁻¹ from the A1 to A5 glass-ceramics gradually narrowed, indicating that a decrease in the SiO₂/B₂O₃ ration reduced the formation of the [BO₃] units in the glass-ceramics. The glass-ceramics produced new signal peaks because the crystalline phases were trended to form glassy phases during the heat treatment [17].

Table 3. Vibrating groups of glasses and glass-ceramics.

Wave number (cm⁻¹)	Corresponding characteristic vibration
466	Bending vibration of O-Si-O in [SiO₄]
543 – 550	Vibration of [AlO₆]
700 – 703	Bending vibration of B-O-B in [BO₃]
1020	Asymmetric vibration of Si-O-Si in [SiO₄]
1087	Asymmetric stretching vibration of Si-O-Si in [SiO₄]
1240 – 1257	Bending vibration of B-O in [BO₃]
1385	Vibration of B-O in [BO₃]

²⁹Si MAS NMR spectroscopy

Figure 4 shows the ²⁹Si MAS NMR spectrum of the parent glasses. The chemical environment of the different Si⁴⁺ caused the corresponding chemical shifts in the ²⁹Si MAS NMR to be different. Therefore, the corresponding unit could be determined by judging the peak positions of the different chemical shifts in the nuclear magnetic resonance test. In silica-based glass, Si could be coordinated 4 times by O to form a tetrahedral structure. Due to the different numbers of bridging oxygen atoms, the tetrahedral might exist in the form of [SiO₄⁴⁻], [Si₂O₇⁶⁻], [SiO₃²⁻], [Si₂O₅²⁻], [SiO₂] [24]. These units could also be expressed in the form of Qⁿ, corresponding to n = 0, 1, 2,

3, 4, respectively [25]. Where Q represents the symmetry of the SiO₄ tetrahedron, and n represents the number of oxygen bridges between each unit. It can be seen from Figure 4 that the ²⁹Si MAS NMR spectroscopies of the parent glasses were mainly concentrated in the range of -75 – -90 ppm. The peak around -70 ppm corresponded to the Q⁰, the peaks produced by the Q¹ were mainly concentrated in -75 – -80 ppm, Q² concentrated in -80 – -85 ppm, Q³ concentrated in -90 – -100 ppm, Q⁴ concentrated in -113 ppm [24-27]. Therefore, there were Q¹, Q², and Q³ in the A1 to A5 parent glasses, and there was no sign of Q⁰ and Q⁴. The Qⁿ unit in the A1 parent glass mainly existed in the form of Q¹ and Q². The resonance peak intensity of Q¹ in the A2 parent glass was weakened, but the resonance peak intensity of Q² was enhanced. This meant that a decrease in the SiO₂/B₂O₃ ratio made the Qⁿ unit inside the glass tend to exist in the form of Q². With a further decrease in the SiO₂/B₂O₃ ratio, Q¹ in the A3 parent glass disappeared and a small amount of Q³ was formed, and Q³ in the A4 and A5 parent glasses gradually increased. Therefore, a further decrease in the SiO₂/B₂O₃ ratio promoted the Qⁿ unit in the glass to exist in the form of Q² and Q³.
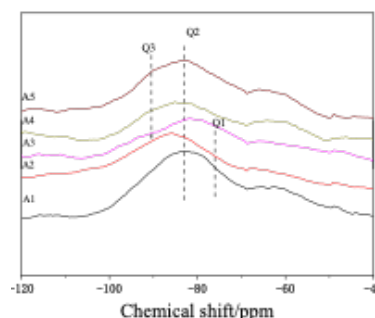

Figure 4. ²⁹Si MAS NMR spectrum of the parent glasses.

XRD analysis

Figure 5 shows the XRD diffraction patterns of the A1 – A5 glass-ceramics sintered at 670 °C and the A3 glass-ceramics sintered at different temperatures. It can be seen that there were faint diffraction peaks in the XRD diffraction patterns. The main diffraction peak positions of the A1 and A2 glass-ceramics were basically the same, but the diffraction peak of the A2 glass-ceramic was stronger than that of the A1 glass-ceramic. However, the main peak position changed from the A3 glass-ceramic, the original diffraction peaks basically disappeared, and a weak diffraction peak appeared at the new position. The diffraction peak in the A4 glass-ceramic was stronger than in the A3 glass-ceramic, but weaker in the A5 glass-ceramic. By comparing the PDF cards, it was found that the crystal phases precipitated in the A1 and A2 glass-ceramics were CaSiO₃

[PDF:72-2297] and SiO_2 [PDF:65-466]. While there was only a single crystal phase $CaSiO_3$ in the A1 glass-ceramic, and only a single crystal phase SiO_2 in the A3-A5 glass-ceramics.
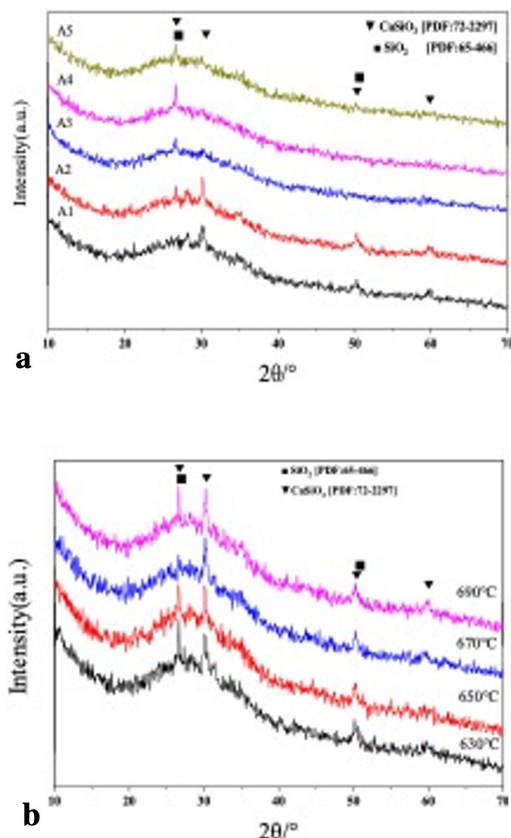

Figure 5. a) XRD of the A1 – A5 glass-ceramics sintered at 670 °C, b) XRD of the A3 glass-ceramics sintered at different temperatures.

Figure 5(b) shows that the crystal phase of the A3 glass-ceramics sintered at different temperatures did not change, all the phases were SiO_2. The different sintering temperatures affected the growth of crystals in the A3 glass-ceramic, and the crystal content was highest when the sintering temperature was 670 °C. From the XRD diffraction pattern analysis, it can be seen that a decrease in the SiO_2/B_2O_3 ratio within a certain range in this glass system enhances the precipitation of $CaSiO_3$. After exceeding this range, a decrease in the SiO_2/B_2O_3 is unfavourable for the precipitation of $CaSiO_3$ and enhances the precipitation of SiO_2. It can be seen from the ^{29}Si MAS NMR spectroscopy that there were Q^1 and Q^2 units in the A1 and A2 parent glasses. The more bridging oxygens in the Q^n unit, the stronger glassiness of the sample. The glassiness was not conducive to the crystallisation of glass during sintering. A decrease in the SiO_2/B_2O_3 ratio changed the Q^n unit in the parent glasses, from the form of Q^1 and Q^2 to the form of Q^2 and Q^3. This result led to a reduction in the crystal phase in the glass-ceramics.

Analysis of the physical and chemical properties

The bending strength of the sintered strip samples reflects the strength of the sintered paste containing this glass, the density reflects the compactness of the paste layer after sintering, and the acid resistance reflects the chemical stability of the paste layer after sintering.

Figure 6 shows the bending strength, density and acid resistance of the A1 – A5 glass-ceramics sintered at 670 °C. It can be seen from Figure 6 that when the SiO_2/B_2O_3 ratio was 0.29, the bending strength and density reached the maximum. The bending strength of the samples was distributed between 34 MPa and 49 MPa. The density was distributed between 2.549 $g \cdot cm^{-3}$ and 2.874 $g \cdot cm^{-3}$. With a decrease in the SiO_2/B_2O_3 ratio, the bending strength first increased slightly and then significantly increased. The maximum bending strength of the A1 – A5 glass-ceramics was 48.6 MPa. After the SiO_2 content exceeded 12 wt. %, the bending strength first decreased slightly and then significantly decreased. The change in the density of the A1 – A5 glass-ceramics was different from the change in the bending strength. Before the SiO_2 reached 12 wt. %, the density of the glass-ceramics increased uniformly with the decrease in the SiO_2/B_2O_3 ratio. After the SiO_2 content exceeded 12 wt. %, the density substantially decreased uniformly. The density and bending strength have a certain proportional relationship. The greater the density, the greater the bending strength will be, so the density and bending strength properties of the samples will have similar changes.
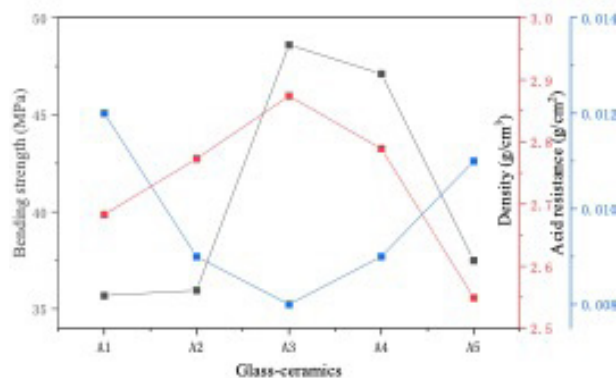

Figure 6. Physical and chemical properties of the A1 – A5 glass-ceramics sintered at 670 °C.

The acid resistance of the glass-ceramics increased uniformly first and then decreased uniformly with the decrease in the SiO_2/B_2O_3 ratio. It can be seen from Figure 6 that the acid resistance reached 0.0081 $g \cdot cm^{-2}$ in the A3 glass-ceramic. The acid resistance of the A1 – A5 glass-ceramics was in the range of 0.0081 – 0.0122 $g \cdot cm^{-2}$.

It can be seen from the structural analysis of the glasses and glass-ceramics above that when the SiO_2/B_2O_3 ratio was 0.29, the $[AlO_6]$ unit disappeared, and the Q^n unit changed from the coexistence of Q^1 and Q^2 to Q^2 and a small amount of Q^3 unit. The crystal phase became a single SiO_2. These structural changes led to the gradual increase in the density, bending strength and acid resistance of the glass-ceramics. As the Q^3 unit and SiO_2 crystal phases gradually increased, the performance of the glass-ceramics began to decline. This result means that when the content of Q^3 unit and SiO_2 crystal phases exceeded a certain amount, it was not conducive to an improvement in the glass-ceramic performance.

Table 3. Physical and chemical properties of the A1 – A5 glass-ceramics sintered at 670 °C.

Number	A1	A2	A3	A4	A5
Bending strength (MPa)	35.679	35.954	48.602	47.113	37.494
Density (g.cm⁻³)	2.683	2.773	2.874	2.789	2.549
Acid resistance (g.cm⁻²)	0.012	0.009	0.008	0.009	0.011

Analysis of SEM and EDS

Figure 7 shows the SEM of the A1 – A5 glass-ceramics sintered at 670 °C after the acid resistance test. After being eroded by HCl, many erosion pits formed on the surface of the samples. With a decrease in the SiO_2/B_2O_3 ratio, the HCl corrosion intensity on the samples changed. The surface layer of the A1 glass-ceramic largely disappeared after being eroded. The original surface of the sample was no longer visible, only rough corrosion pits. The eroded area of the A2 glass-ceramic became a specific round pit, the surface of the round pit became smooth, and the acid resistance improved. In addition, a small amount of crystalline phase could be seen on the surface of the A2 glass-ceramic after being eroded. Comparing with the A2 glass-ceramic, the size of the round pits on the surface of the A3 glass-ceramic after being eroded became smaller, and the acid resistance was further enhanced. A decrease in the acid resistance of the A4 glass-ceramic led to denser corrosion pits than the A3 glass-ceramic after being eroded. The surface of the A5 glass-ceramic was eroded over a large area similar to the A1 glass-ceramic. It can be seen from the crystal phase change of the A1 – A5 glass-ceramics, that the increase in the $CaSiO_3$ content of the crystal phase enhanced the acid resistance of the glass-ceramic, and an increase in the SiO_2 crystal phase reduced the acid resistance of the glass-ceramic.
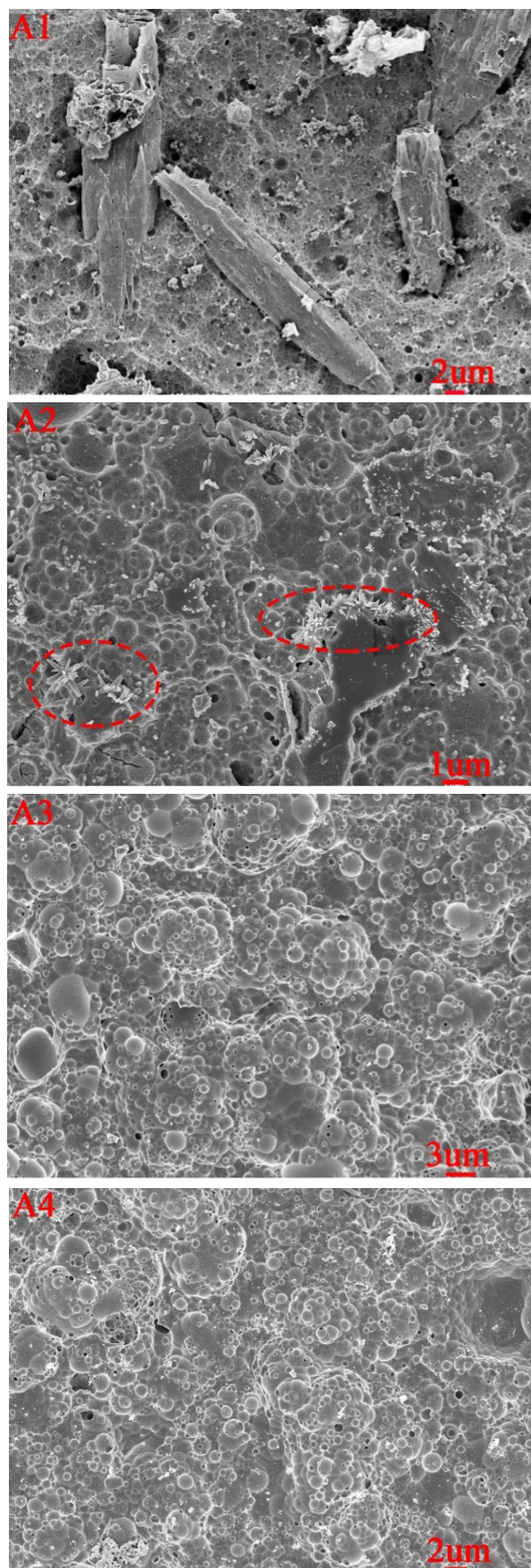

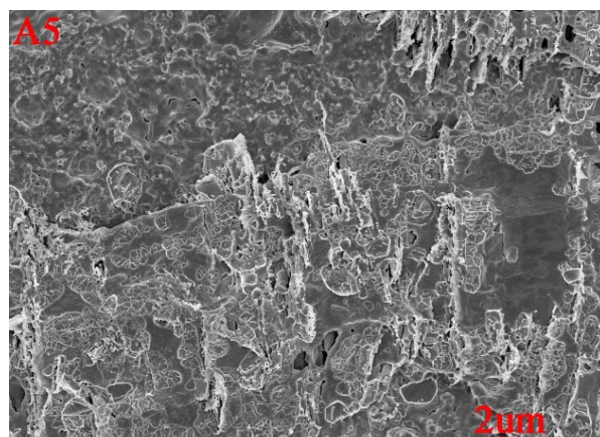Figure 7. SEM images of the A1 – A5 glass-ceramics etched by HCl.

Figure 7. SEM images of the A1 – A5 glass-ceramics etched by HCl.

Figure 8 shows the EDS spectrum of the A3 glass-ceramic sintered at 670 °C before and after acid etching, where (a') corresponds to the EDS of the sample surface before acid etching, (a) (b) (c) correspond to the point or area of the sample after acid etching. It can be seen from the scanned image that the surface of the A3 glass-ceramic before being eroded was smooth. The selected area of the A3 glass-ceramic was glassy phase before the

acid etching, and no crystal phase was found after the acid etching. This was because there were too few crystalline phases to be found in the selected area. The composition of the surface of the A3 sintered glass before and after the acid etching did not change, however, the element content changed. After the acid attack, the Zn and Na content decreased significantly. Obviously, the erosion that the HCl caused on this series of glass-ceramics was mainly due to the erosion of the Zn and Na elements.

CONCLUSIONS

The experimental results show that a decrease in the SiO_2/B_2O_3 ratio reduced the glass transition temperature, but had little effect on the crystallisation temperature. According to the infrared and ^{29}Si MAS NMR analysis, the decrease in the SiO_2/B_2O_3 ratio gradually shifted the absorption peak at 1385 cm^{-1} to the lower band, and the absorption peak at 550 cm^{-1} disappeared. The Q^n unit in glass gradually changed from the coexistence of Q^1 and Q^2 to the coexistence of Q^2 and Q^3. Two new absorption peaks of 466 cm^{-1} and 1087 cm^{-1} were generated in the infrared absorption peak of the glass-ceramics, and the other absorption peaks also changed slightly. With
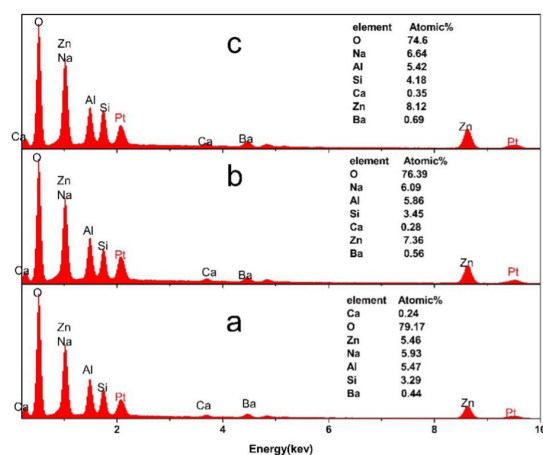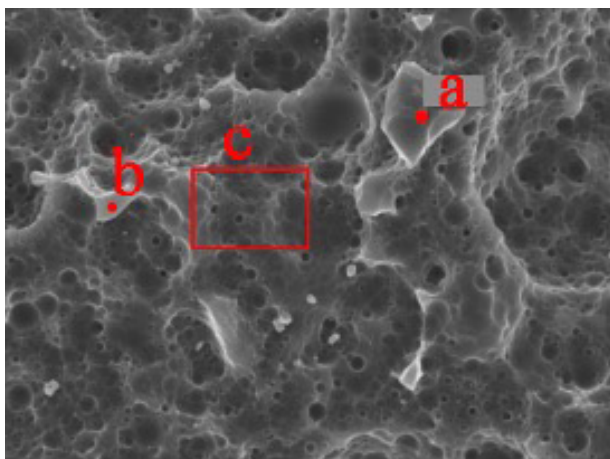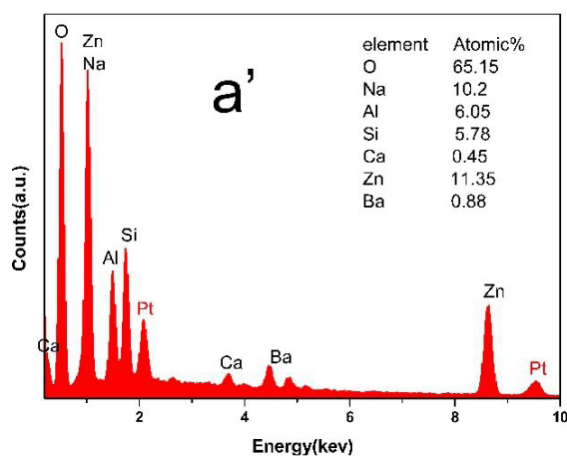

Figure 8. SEM images of the A3 glass-ceramic before and after etching by HCl, EDS spectra of a'), a), b) and c).

a decrease in the SiO_2/B_2O_3 ratio, the crystalline phase of the glass-ceramics gradually transformed from $CaSiO_3$ to SiO_2. The XRD diffraction peaks of the A3 glass-ceramics were the most obvious when the sintering temperature was 670 °C. The physical and chemical properties of the glass-ceramics sintered at 670 °C reached the maximum when the SiO_2/B_2O_3 ratio was 0.29. The bending strength reached 48.602 MPa, the density reached 2.874 g·cm⁻³, and the acid resistance reached 0.008 g·cm⁻². Through the SEM analysis, it could be seen that the corrosion pits on the glass ceramic surface after the HCl corrosion decreases with an increase in the acid resistance, and the erosion pits increased with the weakening of the acid resistance. The erosion of HCl on this series of glass-ceramics was mainly due to the erosion of the Zn and Na elements.

Acknowledgment

REFERENCES

1. Dong Q., Huang C., Duan G. J, Zhang F., Yang D. A. (2017):Facile synthesis and electrical performance of silica-coated copper powder for copper electronic pastes on low temperature co-fired ceramic. *Materials Letters, 186*, 263-266. doi:10.1016/j.matlet.2016.09.116

2. Pham L. Q., Sohn J. H., Park J. H., Kang H. S., Lee B. C., Kang Y. S. (2011): Comparative study on the preparation of conductive copper pastes with copper nanoparticles prepared by electron beam irradiation and chemical reduction. *Radiation Physics and Chemistry, 80*, 638-642. doi: 10.1016/j.radphyschem.2011.01.004

3. Wu S. P. (2007):Preparation of ultra-fine copper powder and its lead-free conductive thick film. *Materials Letters, 61*, 3526-3530. doi:10.1016/j.matlet.2006.11.128

4. Clement C., Bell H., Vogg F., Rebenklau L., Gierth P., Partsch U. (2013): Inert Drying System for Copper Paste Application in PV. *Energy Procedia, 38*, 423-429. doi:10.1016/j.egypro.2013.07.299

5. Xu X., Zhuang H., Li W., Jang G. (2004): Bonding behavior of copper thick films containing lead-free glass frit on aluminum nitride substrates. *Ceramics International, 30*, 661-665. doi:10.1016/j.ceramint.2003.07.012

6. Kraft A., Nil, Kalio A., Moldovan A., Bartsch J., Glatthaar M., W. Glunz S. (2013): Influence of the chemicals used in nickel and copper plating solutions on the adhesion of screen-printed silver contacts. *Energy Procedia, 38*, 753-759. doi:10.1016/j.egypro.2013.07.343

7. Yoshida M., Tokuhisa H., Itoh U., Kamata T., Sumita I., Sekine S. (2012): Novel Low-Temperature-Sintering Type Cu-Alloy Pastes for Silicon Solar Cells. *Energy Procedia, 21*, 66-74. doi:10.1016/j.egypro.2012.05.009

8. Zhou J., Xu N., Yang H., Zhang Q. (2014): Effect of Ag Powder and Glass Frit in Ag Paste on Front Contact of Silicon Solar Cells. *Procedia Engineering, 94*, 1-5. doi:10.1016/j.proeng.2013.10.007

9. Guo W., Fu L., He P., Lin T., Wang C. (2019): Crystallization and wetting behavior of bismuth-borate-zinc glass and its application in low temperature joining alumina ceramics. *Journal of Manufacturing Processes, 39*, 128-137. doi: 10.1016/j.jmapro.2019.02.019

10. Kumar U. (2002): A development methodology for copper end termination paste – part 1 origin of green defects. *Active and Passive Electronic Components, 25*, 169-179. doi: 10.1080/08827510212348

11. Yang W. C., Sun Q., Lei Q., Zhu W. B., Li Y. F., Wei J., Li M. Y. (2019): Formation of a highly conductive thick film by low-temperature sintering of silver paste containing a Bi₂O₃-B₂O₃-ZnO glass frit. *Journal of Materials Processing Technology, 267*, 61-67. doi: 10.1016/j.jmatprotec.2018.09.029

12. Luo X. F., Ren L. C., Xia Y. S., Hu Y. K., Gong W. Y., Cai M. C., Zhou H. Q. (2017):Microstructure, sinterability and properties of CaO-B₂O₃-SiO₂ glass/Al₂O₃ composites for LTCC application. *Ceramics International, 43*, 6791-6795. doi: 10.1016/j.ceramint.2017.02.096

13. Qin Y., Zhong C., Yang H., Qin T., Yuan Y., Tang B., Zhang S. (2019): Enhanced thermal and mechanical properties of Li–Al–Si composites with K₂O–B₂O₃–SiO₂ glass for LTCC application. *Ceramics International, 45*, 15654-15659. doi: 10.1016/j.ceramint.2019.05.077

14. Wang S. F., Hsu Y. F., Lu H. C., Lo S. C., Cheng C. S. (2012): B₂O₃-free SiO₂-Al₂O₃-SrO-La₂O₃-ZnO-TiO₂ glass sealants for intermediate temperature solid oxide fuel cell applications. *International Journal of Hydrogen Energy, 37*, 5901-5913. doi: 10.1016/j.ijhydene.2011.12.121

15. Luo X. F., Ren L. C., Hu Y. K., Xia Y. S., Xin M., Zhang C., Zhou H. Q. (2018): Fabrication and performance of dielectric tape based on CaO-B₂O₃-SiO₂ glass/Al₂O₃ for LTCC applications. *Ceramics International, 44*, 6354-6361. doi: 10.1016/j.ceramint.2018.01.026

16. Wang. T, He Y., Liang Z. Y., Cui X. M. (2015): Preparation of LTCC materials with adjustable permittivity based on BaO-B₂O₃-SiO₂/BaTiO₃ system. *Materials Research Bulletin, 65*, 249-252. doi: 10.1016/j.materresbull.2015.02.009

17. Shi J., He F., Xie J., Liu X., Yang H. (2019):Effect of heat treatments on the Li₂O-Al₂O₃-SiO₂-B₂O₃-BaO glass-ceramic bond and the glass-ceramic bond cBN grinding tools. International Journal of Refractory *Metals and Hard Materials, 78*, 201-209. doi: 10.1016/j.ijrmhm.2018.09.015

18. He F., Wang J., Deng D. W. (2011): Effect of Bi₂O₃ on structure and wetting studies of Bi₂O₃-ZnO-B₂O₃ glasses. *Journal of Alloys and Compounds, 509*, 6332-6336. doi: 10.1016/j.jallcom.2011.03.087

19. Kaur K., Singh K. J., Anand V. (2016): Structural properties of Bi₂O₃-B₂O₃-SiO₂-Na₂O glasses for gamma ray shielding applications, *Journal of Radiation Physics and Chemistry, 120*, 63-72. doi: 10.1016/j.radphyschem.2015.12.003

20. Kaur R., Singh S., Pandey O. P. (2013): Absorption spectroscopic studies on gamma irradiated bismuth borosilicate glasses. *Journal of Molecular Structure, 1049*, 386-391. doi: 10.1016/j.molstruc.2013.06.056

21. Chen M., He F., Shi J., Xie J., Yang H., Wan P. (2019): Low Li₂O content study in Li₂O-Al₂O₃-SiO₂ glass-ceramics, *Journal of the European Ceramic Society, 39*, 4988-4995. doi: 10.1016/j.jeurceramsoc.2019.07.032

22. Salinigopal M. S., Gopakumar N., Anjana P. S., Pandey O. P. (2020): Synthesis and characterization of 50BaO - (5-x) Al$_2$O$_3$ - xR$_2$O$_3$ - 30B$_2$O$_3$ - 15SiO$_2$(R = Nd, Gd) glass-ceramics. *Journal of Non-Crystalline Solids, 535*, 119956. doi: 10.1016/j.jnoncrysol.2020.119956

23. Gao X. L., Zhang Q., Yu J. B., Tang W. F, Li Y. X., Lu A. X. (2018): Effect of replacement of Al$_2$O$_3$ by Y$_2$O$_3$ on the structure and properties of alkali-free boro-aluminosilicate glass. *Journal of Non-Crystalline Solids, 481*, 98-102. doi: 10.1016/j.jnoncrysol.2017.10.032

24. Silva A. M. B., Queiroz C. M., Agathopoulos S., Correia R. N., Fernandes M. H. V., Oliveira J. M. (2011): Structure of SiO$_2$-MgO-Na$_2$O glasses by FTIR, Raman and ^{29}Si MAS NMR. *Journal of Molecular Structure, 986*, 16-21. doi: 10.1016/j.molstruc.2010.11.023

25. Aguiar H., Solla E. L., Serra J., González P., León B., Malz F., Jäger C. (2008): Raman and NMR study of bioactive Na$_2$O-MgO-CaO-P$_2$O$_5$-SiO$_2$ glasses, *Journal of Non-Crystalline Solids, 354*, 5004-5008. doi: 10.1016/j.jnoncrysol.2008.07.033

26. Elgayar I., Aliev A. E., Boccaccini A. R., Hill R. G. (2005): Structural analysis of bioactive glasses. *Journal of Non-Crystalline Solids, 351*, 173-183. doi: 10.1016/j.jnoncrysol.2004.07.067

27. Ma J. J., Wang M., You J. L., Tang K., Lu L. M., Wan S. M., Wang J., Gong X. Y., Wang Y. C. (2020): Quantitative studies on the structure of xCaO center dot(1-x)SiO2 glasses and melts by in-situ Raman spectroscopy, ^{29}Si MAS NMR and quantum chemistry ab initio calculation. *Journal of Non-Crystalline Solids, 546*, 120252. doi: 10.1016/j.jnoncrysol.2020.120252